Publ. Astron. Soc. Japan (2014) 66 (SP1), S4 (1–14)
doi: 10.1093/psu/psu082
Advance Access Publication Date: 2014 November 27

The solar cycle dependence of the weak internetwork flux

Bruce W. Lites,*,† Rebecca Centeno, and Scott W. McIntosh

High Altitude Observatory/National Center for Atmospheric Research, P.O. Box 3000, Boulder, CO 80307, USA

*E-mail: lites@ucar.edu

†Visiting Professor, National Observatory of Japan, 2-21-1 Osawa, Mitaka, Tokyo 181-8588, Japan

Received 2014 February 21; Accepted 2014 May 1

Abstract

We examine data from the Hinode Observing Program 79 (the "HOP 79" irradiance program) as observed using the Hinode Solar Optical Telescope Spectro-Polarimeter for systematic changes in the weakest observable magnetic flux during the period 2008–2013. At moderate latitudes we find no evidence for systematic changes as a function of time and solar latitude in either the unsigned line-of-sight flux or in the measures of the transverse flux. However, in the polar regions, changes are apparent in the measure of signed magnetic flux corresponding to reversal of the polarity of the poles, changes that persist even for the weakest observed flux. Also evident in measures of the weakest signed flux are preferences for positive (negative) polarity at mid-north (mid-south) latitudes (20°–60°). Center-limb variations in various measures of the weak flux appear to be independent of the solar cycle. The results are consistent with the operation of a small-scale solar dynamo operating within and just below the solar photosphere, but the measures of the weakest signed flux still contain small signatures of the global solar cycle.

Key words: Sun: activity — Sun: magnetic fields — Sun: photosphere

1 Introduction

Synoptic maps derived from full-disk solar magnetograms (i.e., the "magnetic butterfly diagrams," Hathaway 2010; see figure 1) reveal that the solar cycle manifests itself in the quiet Sun, albeit in a manner distinct from that of solar active regions. When displayed on the largest scales, quiet Sun regions at latitudes greater than the sunspot emergence zones (±40°) show episodic regions dominated by the magnetic polarity opposite to that of the polar fields in the corresponding hemisphere. These regions, whose higher latitude extent corresponds to the location of the polar crown filaments, appear to "rush to the poles" (Waldmeier 1960; Hyder 1965) as the cycle progresses. It has been speculated that remnant fields of dispersed active regions are carried toward the poles by diffusion (Leighton 1964) and/or by large-scale meridional circulation not far below the solar surface (Babcock 1961; Howard & Labonte 1981; Wang et al. 1989). These migrating fields progressively appear to "cancel" the polar fields, eventually leading to reversal of the polar polarity some years after the onset of the active region cycle at lower latitudes. Thus it seems that non-sunspot magnetic fields, or at least fields remnant from active regions, play an integral role in the solar cycle. Other processes, instead of or in addition to diffusion and meridional circulation, may be responsible for explaining the apparent poleward migration of the large-scale fields and reversal of the polar polarity (e.g., Ulrich & Tran 2013).

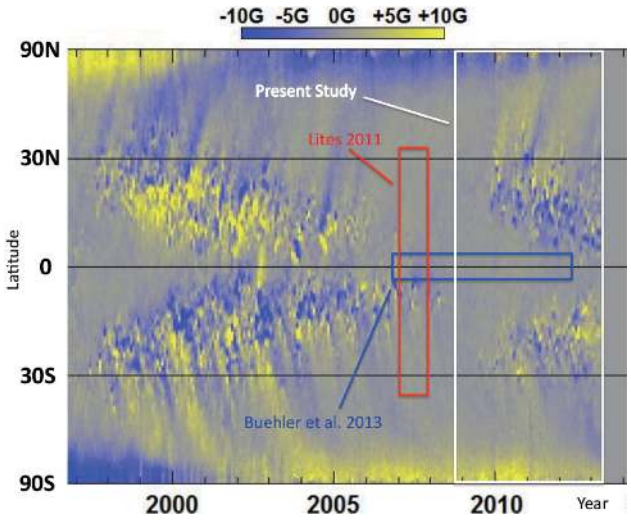

Fig. 1. A recent portion of the NASA "magnetic butterfly diagram" (Hathaway 2010) is presented showing magnetographic signals and polarities over the most recent solar cycle (see color key at top). The evolutionary patterns resulting from the global solar cycle are clearly evident. The superimposed red and blue rectangles indicate the approximate coverage of studies of weak internetwork flux using Hinode SOT/SP data (Lites 2011; Buehler et al. 2013, respectively). The white rectangle indicates the coverage of the data used in the present work.

It is important to understand the origin and nature of this poleward-migrating quiet Sun flux in order to confront a number of issues regarding its connection to the solar cycle: Is the imbalance in the flux confined to kilogauss fields, or does it persist even at the weakest flux levels detectable? If the imbalance is confined mainly to the strongest fields, then those "unipolar" fields are likely the remnants of active regions. If it persists to the weakest fields then it may arise from some deeper-seated process.

In this paper we question what, if any, signatures of the global solar cycle are carried by the weakest observable components of quiet Sun magnetic flux. We isolate the weak components, then search for any behavior of these fields that persists at larger spatial scales and over time. There have been few studies to date that have attempted to describe the long-term or large-scale behavior of internetwork (that is, outside of the solar magnetic network elements—hereafter IN) fields in the quiet Sun. Sánchez Almeida (2003) compared two magnetographic observations obtained near the center of the disk at solar minimum and solar maximum. He found that the IN fields had similar values of unsigned magnetic flux density in the two epochs, but his result was derived from observations of two different instruments, obtained at two different telescopes, and under different observing conditions.

A completely different approach to variations with the solar cycle was described by Shchukina and Trujillo Bueno (2003), where they analyze scattering polarization in Sr I 460.7 nm. Comparing observations near the limb at the minimum and maximum of the solar cycle, and using detailed numerical modeling as a guide, they infer a turbulent magnetic field strength in the quiet Sun of about 60 G during both epochs. Although they could not distinguish between network and IN regions, they argue that the area of IN dominates by a large factor. The contributions to alteration of the scattering polarization from the Hanle effect should be in approximate proportion to the areas of IN and network, so in so far as the Hanle effect diagnostic in Sr I 460.7 nm represents photospheric fields of the quiet Sun, no substantial change was noted from minimum to maximum of the cycle. More recently, Kleint et al. (2010) used the Hanle effect for linear polarization near the limb in C_2 molecular lines, supplemented by Stokes *V* signals from nearby Fe I lines, to search for solar-cycle-related variations in the intrinsically weak fields of the quiet Sun. The fields so inferred show only a slight possible decrease during the decay phase of solar cycle 23.

With the advent of the Hinode spacecraft in late 2006, it became possible to make precision measures of very weak polarization signatures from magnetic fields in the quiet photosphere with consistently high angular resolution and high polarimetric precision. Lites (2011) used the Hinode Solar Optical Telescope Spectro-Polarimeter (SOT/SP) to study weak IN fields as a diagnostic for the presence or absence of small-scale turbulent dynamo action. The extensive observations used in that study covered a range of solar latitudes, but was confined to observations during 2007 (the red rectangle of figure 1). Recently, Buehler, Lagg, and Solanki (2013) used Hinode SOT observations to examine the solar cycle dependence of quiet Sun fields near disk center by examining distributions of both circular and linear polarization at various epochs (the blue rectangle in figure 1). They found no significant variation of the distribution functions or of the properties of magnetic patches having flux $< 10^{19}$ Mx during that period. They argue, as did Lites (2011), that their results are consistent with the operation of a small-scale turbulent dynamo.

Hinode SOT/SP measurements of only the polar regions have also been obtained on a regular basis. Shiota et al. (2012) investigated the behavior of the polar fields during the period 2008–2012. They found that, whereas the larger patches of polar magnetic field responsible for the dominant polar polarity vary considerably with the cycle, concentrations of fields with flux $< 10^{18}$ Mx are nearly constant. This behavior suggests that even in the polar regions the internetwork fields arise from a mechanism distinct from the global solar cycle. Of course, these polar measurements do not encompass what may be the most interesting regions for solar cycle dependence of IN magnetism: latitudes from the

upper extent of the sunspot emergence zones to the polar regions that participate in the "rush to the poles."

The aim of the present work is to explore the full range of latitude–time behavior of the weak IN flux using a unique time series of high-resolution, high-sensitivity data obtained on a regular basis since 2008 with the Hinode SOT/SP.

2 Observations

The observations employed for this study were obtained with the Spectro-Polarimeter (Lites et al. 2013) of the Solar Optical Telescope (SOT: Tsuneta et al. 2008) on board the Hinode mission (Kosugi et al. 2007). The SOT/SP records full Stokes I, Q, U, V spectra of the Fe I lines at 630 nm with typical polarization sensitivity of 10^{-3} relative to the continuum intensity.

Every month from 2008 November to the present, the mission has carried out Hinode Observing Program 79 (HOP 79), the "irradiance program," in which measurements are taken with separate spacecraft pointings along the solar central meridian covering all latitudes in the north–south (N–S) direction with observations from both the SOT/SP and the SOT Filtergraph instrument (SOT/FG). HOP 79 provides a unique record of the solar photosphere versus latitude and time at high angular resolution and high polarimetric sensitivity.

The failure of the Hinode high-rate X-band telemetry in late 2007 necessitated limitations on telemetry volume, thereby placing restrictions on data-intensive observations such as HOP 79. One of the requirements of HOP 79 is that both SP and FG observations cover all latitudes in the N–S direction. The small pixel dimensions of the high-resolution FG broadband filter data limit its spatial coverage in the N–S direction to about 109″, so with adequate overlap of each spacecraft pointing in the N–S direction, about 20 separate spacecraft pointings are required to complete the HOP 79 N–S observational sequence. The HOP 79 SOT/SP observations use a window of 816 SOT/SP pixels along the slit (out of a maximum of 1024) in order to limit unnecessary overlap among the separate spacecraft pointing positions. The SOT/SP data are binned onboard by two pixels along the slit (in the N–S direction). However, no summing is carried out in the slit scanning (east–west, E–W) direction, so the HOP 79 SOT/SP data have full angular resolution in that dimension. To further reduce telemetry volume by a factor of two, the HOP 79 program collects only one of the two images of the SOT/SP dual-beam spectropolarimeter (so-called "single-sided" data). The integration time at each slit-scan position is 4.8 s, so each recorded spatial element has a random noise level equal to that of the SOT/SP "normal map." For single-sided data the level of crosstalk from Stokes $I \rightarrow Q$, U, V arising from residual image motion and evolution of the solar scene can be dramatically larger than that of the dual-sided data (Lites 1987; Judge et al. 2004), but owing to the excellent stability of the Hinode/SOT Correlation Tracker (Shimizu et al. 2008) and the empirical correction for $I \rightarrow Q$, U, V crosstalk in the SP_PREP data reduction package (Lites & Ichimoto 2013), the influence of this source of error is greatly reduced to the point that it is comparable to the random noise level of the observations. Each HOP 79 SOT/SP map of [190, 408] observation elements has a field of view of [28.″2, 130.6] in [x, y].

This study comprises 52 monthly HOP 79 sequences, 990 SOT/SP maps in total, spanning from the beginning of uniform HOP 79 data acquisition in 2008 October through 2013 May. The observing mode is uniform for these data, so except for a slight degradation in instrumental throughput of about 20% and possible slight departures in instrumental focus among the observational data sets (see subsection 4.2), the data are of uniform angular resolution and sensitivity.

3 Data reduction

We employ the SOT/SP data that has been processed by the routine data reduction processing package SP_PREP (Lites & Ichimoto 2013). SP_PREP produces level1 (calibrated Stokes spectra) and level2 (results of a least-squares Milne–Eddington inversion procedure). Because we are interested primarily in the weakest field component of the quiet Sun, we do not use level2 data in this paper. Rather, we use the measures of wavelength-integrated circular and linear polarization in the Fe I 630 nm lines as proxies of the magnetic field longitudinal and transverse to the line-of-sight, respectively. The level1 processing supplies these measures as "quick look" data products. The wavelength-integrated measures of line polarization are described in Lites et al. (2008). They are best suited to description of the longitudinal ($B^L{}_{\rm app}$) and transverse ($B^T{}_{\rm app}$) apparent flux density of weak IN fields. The quantity $B^L{}_{\rm app}$ in Lites et al. (2008) differs slightly from that resulting from the SP_PREP processing. Following a suggestion by J. Stenflo, the wavelength-integrated circular polarization $V_{\rm tot}$ entering the calculation of $B^L{}_{\rm app}$ has been modified to

$$V_{\rm tot} = \frac{\int_{\lambda_b}^{\lambda_0} V(\lambda) d\lambda - \int_{\lambda_0}^{\lambda_r} V(\lambda) d\lambda}{(\lambda_r - \lambda_b) I_c}, \quad (1)$$

where I_c is the intensity of the local continuum, λ_0 is the measured wavelength of line center of either of the two Fe I 630 nm lines, and λ_b and λ_r are the blue and red limits of integration, set as [−0.03, +0.03] nm, respectively, from the center of each line. The integrals range

over both Fe I 630 nm lines. Because it employs no absolute value operations, this method of calculating $V_{\rm tot}$ results in no bias when the signals are dominated by random noise.

The level 1 and level 2 data products for the SOT/SP are provided online[1] to the community for every observed data set.

4 Data analysis

4.1 Pointing corrections

The level1 data contain pointing coordinates for every pixel in each SOT/SP map, given in arcsec N–S and E–W of disk center. These coordinates are based upon measured offsets of FG images in regularly scheduled co-alignment verification of the spacecraft pointing using the solar limbs. Several factors contribute to inaccuracy of the SOT/SP pointing information, including drift of the spacecraft pointing over time, thermal drift of the SOT/SP relative to the FG, wandering of the pointing due to the changing solar scene seen by the Hinode/SOT correlation tracker, and a slow drift of the pointing up the strong gradient of continuum intensity near the solar limb. The drift of the SOT pointing near the limb is such that the observed location progresses in the direction toward disk center during a map.

We examine the inferences of magnetic field as a function of position on the solar disk, and also as a function of solar latitude, therefore it is important to have accurate measures of the position on the disk of each observed pixel, and especially so for the HOP 79 SOT/SP maps near to, or including, the solar north or south limbs. In each map that includes the solar limb, we locate the position of the limb in the N–S direction as a function of the slit scan step, then adjust the pointing coordinates of the limb map so that the limb location occurs at the expected value of the solar radius on the date of the observation. Furthermore, we use the average correction in the N–S direction derived from the limb maps to correct the N–S coordinates of those HOP 79 maps in the same sequence that are immediately adjacent to the limb map. Pointing offsets interpolated in time from the closest measurements of the routine co-alignment data are used to correct pointing coordinates for the remainder of the maps in each sequence. Corrections similarly derived from the E–W co-alignment data are applied to each map.

[1] ⟨http://www.csac.hao.ucar.edu/csac/dataHostSearch.jsp⟩.

4.2 Accounting for focus changes among HOP 79 data sets

In examining HOP 79 data obtained near disk center, Buehler, Lagg, and Solanki (2013) noted a temporal variation in the rms granular contrast of the continuum intensity. They attributed those contrast changes to changes in focus of the SOT. To minimize the influence on the weak fields, they applied a convolution to monochromatic images built from the Stokes spectra in order to degrade the effective resolution to a uniform value.

It is entirely plausible that temporal variation of the SOT focus may account for the observed fluctuation of rms continuum contrast. Such focus changes might arise from temperature changes within the spacecraft, as suggested by Buehler, Lagg, and Solanki (2013), but it should also be noted that the focus position of the SOT is set by the daily planner, so one is not assured that the focus relative to the current best focus for the SOT/SP at the time of observation is constant. Indeed, frequently the focus is set to optimize observations for the higher-resolution FG instrument, so that the SOT/SP image may depart substantially from its best focus position. In our analysis we assume that uncompensated movements in focus are slowly varying so that they may be considered constant over the duration of a typical HOP 79 sequence. This assumption is validated by the history of the SOT focus drift over the duration of the mission, where the long-term drift of the best focus position dominates over any shorter-term changes.

We have examined the data and find variations in the rms granular contrast similar to those reported by Buehler, Lagg, and Solanki (2013). Figure 2a shows the rms continuum contrast of the HOP 79 SOT/SP maps as a function of the mean distance of the map from the center of the solar disk. On the disk the rms contrast drops off toward the limb. At a point very close to the limb the steep intensity gradient causes the rms contrast to increase. When the limb itself occurs within the image, the rms fluctuation of the image increases beyond the scale of this plot. In order to minimize the center–limb granular contrast effects in our attempt to determine slowly changing focus drift, we consider in this section only SOT/SP maps within 200″ of the center of the disk. The values of rms contrast derived from these maps near the center of the disk are presumed to be representative of all maps in the same monthly HOP 79 sequence.

Figure 2b presents results for the 203 HOP 79 maps within 200″ of disk center. Typically there are four or five maps within that range for each of the 51 HOP 79 sequences studied. This plot shows the rms granular contrast as a function of time. The data points are indicated by small dots, and the average for each sequence is indicated by a diamond

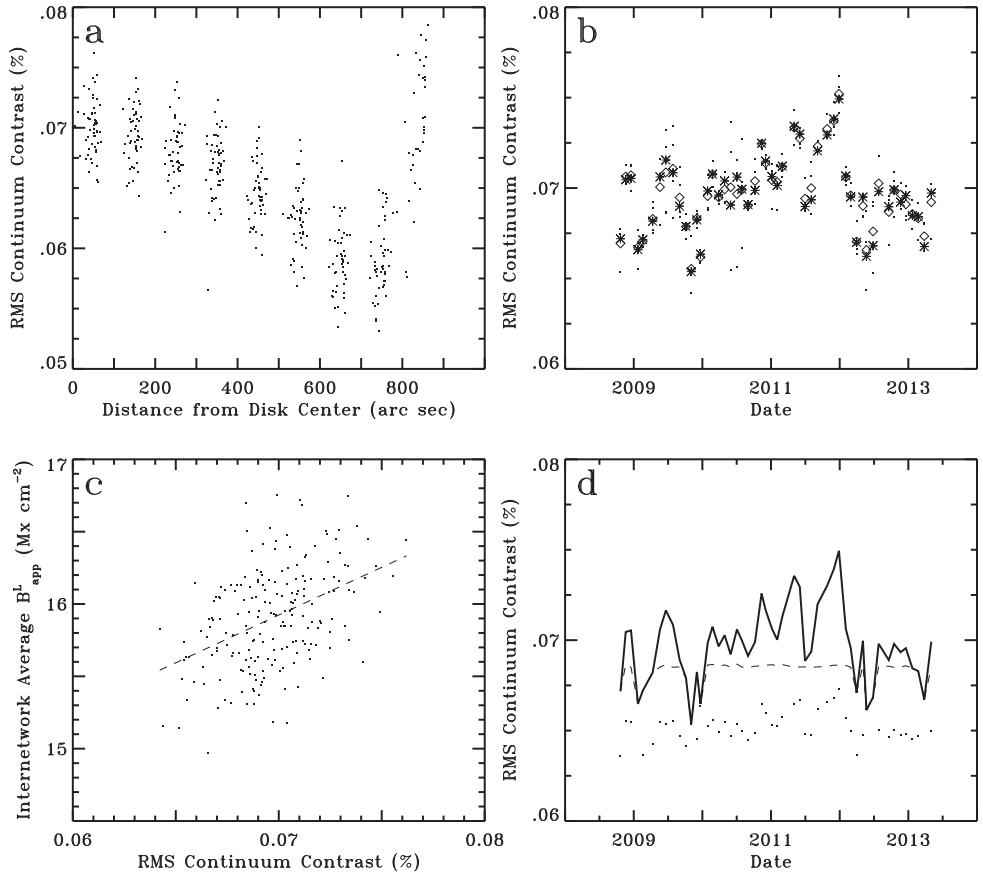

Fig. 2. Properties of the rms continuum contrast for HOP 79 SOT/SP observations are shown. (a) The rms contrast as a function of distance from disk center for all 990 SOT/SP HOP 79 maps. (b) The rms continuum contrast for those maps within 200″ of Sun center as a function of time (dots), with the average rms contrast for each of the 51 HOP 79 sequences shown as diamonds, and the closest of the operations within each sequence to the average of that sequence highlighted as an asterisk. (c) A scatter plot of average B^L_{app} as a function of rms continuum contrast for the 203 SOT/SP maps shown in (b). (d) Average rms continuum contrast for the 51 HOP 79 sequences (solid line), rms contrast of the continuum image after convolution of the image with variable Gaussian smearing to arrive at a mean contrast of 6.85% (dashed line), rms continuum contrast after full convolution of monochromatic images using Gaussian broadening widths resulting in the dashed line (dots).

symbol. The individual measurement closest to the average is shown as an asterisk. From figure 2b it is evident that the fluctuations in rms contrast among sequences is considerably larger than the fluctuation among observations of an individual sequence. To a large extent, variations of the diamonds in this panel parallel those of figure 2 of Buehler, Lagg, and Solanki (2013).

Figure 2c displays the mean longitudinal apparent flux density B^L_{app} of IN regions (see subsection 4.3 below) versus rms continuum contrast for the 203 SOT/SP maps near disk center. We identify a trend in this relationship as indicated by the least-squares linear fit shown as the dashed line. These data verify that some compensation for a possible instrumental effect is warranted.

Following Buehler, Lagg, and Solanki (2013) we degrade all observations spatially using a convolution. For this purpose we adopt a simple Gaussian instrumental broadening function rather than the computed defocus instrument function of Buehler, Lagg, and Solanki (2013). Because the added instrumental broadening is small—about one SOT/SP spatial pixel or half the theoretical resolution limit of the telescope alone at 630 nm—we assume the added broadening of Gaussian shape should be sufficient for the purposes of this study. The results of this convolution are shown in figure 2d for the 51 SOT/SP maps highlighted by asterisks in figure 2b as representative of the focus for each of the 51 HOP 79 sequences. The solid line in figure 2d is the un-convolved variation of rms contrast as a function of time. The dashed line represents the convolution of the continuum intensity only as extracted from the level1 data. The Gaussian widths of the convolution are derived iteratively, and no smearing is applied to the few data sets having rms contrast less than 6.85% before convolution. This lower limit was adopted in order that a smaller spatial smearing is applied for the majority of the sequences. The individual points in figure 2d represent

the rms continuum contrast after assembling monochromatic images for each wavelength, performing the convolution on each monochromatic image, then re-assembling spectra and selecting the continuum intensity. The dots in figure 2d are lower than the dashed line because the operations leading to those results are not equivalent. In the case of the full convolution wavelength-by-wavelength (as is the case for actual observations) there are seven convolutions, one for each of the seven wavelengths entering the average of the continuum intensity. In the case of convolution of the wavelength-averaged continuum intensity (dashed line), only one convolution was applied. The residual fluctuations after the full convolution (dots) are fairly small, with the average rms contrast being about 6.5%. The scatter plot corresponding to figure 2c for the data generated after the full convolution shows no discernible trend.

4.3 Selection of IN regions

The criteria for distinction between network and IN regions is both subjective and dependent upon instrumental angular resolution and sensitivity. For the purposes of the present study we seek to isolate and avoid regions of strong magnetic flux. Following the selection criterion of Lites (2011) for Hinode SOT/SP data of the quiet IN, we choose to consider the "Network" as any location having $|B^L{}_{\rm app}| > 100\,{\rm Mx\,cm^{-2}}$, and eliminating pixels within 2″ of these higher-strength fields (hereafter "Bloom" regions). It avoids a bloom of polarized light arising from scattering in the instrument. This very conservative Bloom designation excludes high-flux regions and their surroundings as indicated by the black ovals in the right panels of figure 3. The data chosen for this illustration are from the north limb and disk center. The continuum images on the left show the unequal horizontal and vertical spatial sampling. The middle and right panels of figure 3 display the measured $B^L{}_{\rm app}$ as color images. For the rightmost images, all pixels with signals $< 3\,\sigma$ (where σ is the rms noise of the disk-center measurement, $2.4\,{\rm Mx\,cm^{-2}}$) are displayed as white. We flag pixels with $20 \le |B^L{}_{\rm app}| \le 100\,{\rm Mx\,cm^{-2}}$ with green, and strong transverse flux regions ($B^T{}_{\rm app} > 170\,{\rm Mx\,cm^{-2}}$) with yellow. In the remainder of this article we make the following definitions of quiet Sun regions outside of the designated Bloom regions:

(i) Noise regime, "Noise": $B^L{}_{\rm app} < 7.2\,{\rm Mx\,cm^{-2}}$,
(ii) Internetwork regime, "IN": $7.2 \le |B^L{}_{\rm app}| \le 100\,{\rm Mx\,cm^{-2}}$ and $B^T{}_{\rm app} < 170\,{\rm Mx\,cm^{-2}}$,
(iii) Core internetwork regime, "Core IN" : $20 \le |B^L{}_{\rm app}| \le 100\,{\rm Mx\,cm^{-2}}$ and $B^T{}_{\rm app} < 170\,{\rm Mx\,cm^{-2}}$,
(iv) Weak internetwork regime, "Weak IN": $7.2 \le |B^L{}_{\rm app}| < 20\,{\rm Mx\,cm^{-2}}$ and $B^T{}_{\rm app} < 170\,{\rm Mx\,cm^{-2}}$.

Table 1. Fractional areas.

	Weak IN	Core IN	All IN	Noise	Bloom
Center	0.141	0.039	0.179	0.615	0.205
Limb	0.225	0.034	0.258	0.726	0.010

In this study the Noise regions, identified by white areas in figure 3, are excluded from the analysis. The strong transverse flux regions (yellow) mainly isolate concentrations of vertically oriented strong flux (Tsuneta et al. 2008) when viewed near the poles. The Core IN regions comprise the highest circular polarization signals within the IN.

Table 1 presents the fractional area on the solar disk for the regions distinguished by colors in figure 3. Several facts are apparent in figure 3 and table 1:

(i) The Bloom network regions exclude a significant fraction of the area near the center of the disk, but are nearly absent close to the limb because the network fields are oriented close to the local vertical, thereby presenting the observer with stronger horizontal rather than vertical flux.
(ii) The Noise regions dominate the IN area. The noise cutoff is conservative, but it ensures that there is minimal contribution to the diagnostics presented in this paper, even at the limb where the measurement noise is higher than at disk center.
(iii) The Core IN regions occupy only a small fraction of the area designated as IN, but contain about 63% of the IN flux. They tend to occur in isolated, small-scale patches surrounded by halos of weaker apparent flux density (the Weak IN flux).
(iv) Very few locations near the center of the disk exceed the transverse flux limit, $B^T{}_{\rm app} > 170\,{\rm Mx\,cm^{-2}}$.
(v) The fractional area coverage of Weak IN flux is significantly larger near the limb than at disk center, probably because of foreshortening.
(vi) Near the limb, some patches of stronger flux appear to survive the exclusion criteria for network. These patches are flagged green as Core IN, or with yellow for strong transverse flux ($B^T{}_{\rm app} > 170\,{\rm Mx\,cm^{-2}}$).
(vii) Near the limb the Weak IN regions have less tendency than at disk center to surround Core IN.

5 Synoptic maps for unsigned longitudinal apparent flux density

First we examine the data record of the *unsigned* longitudinal apparent flux density $|B^L{}_{\rm app}|$, as displayed in the "synoptic maps" of figure 4. The aim is to seek signatures of the large-scale magnetism of the solar cycle in the weakest components of IN magnetic fields. The analysis leading to

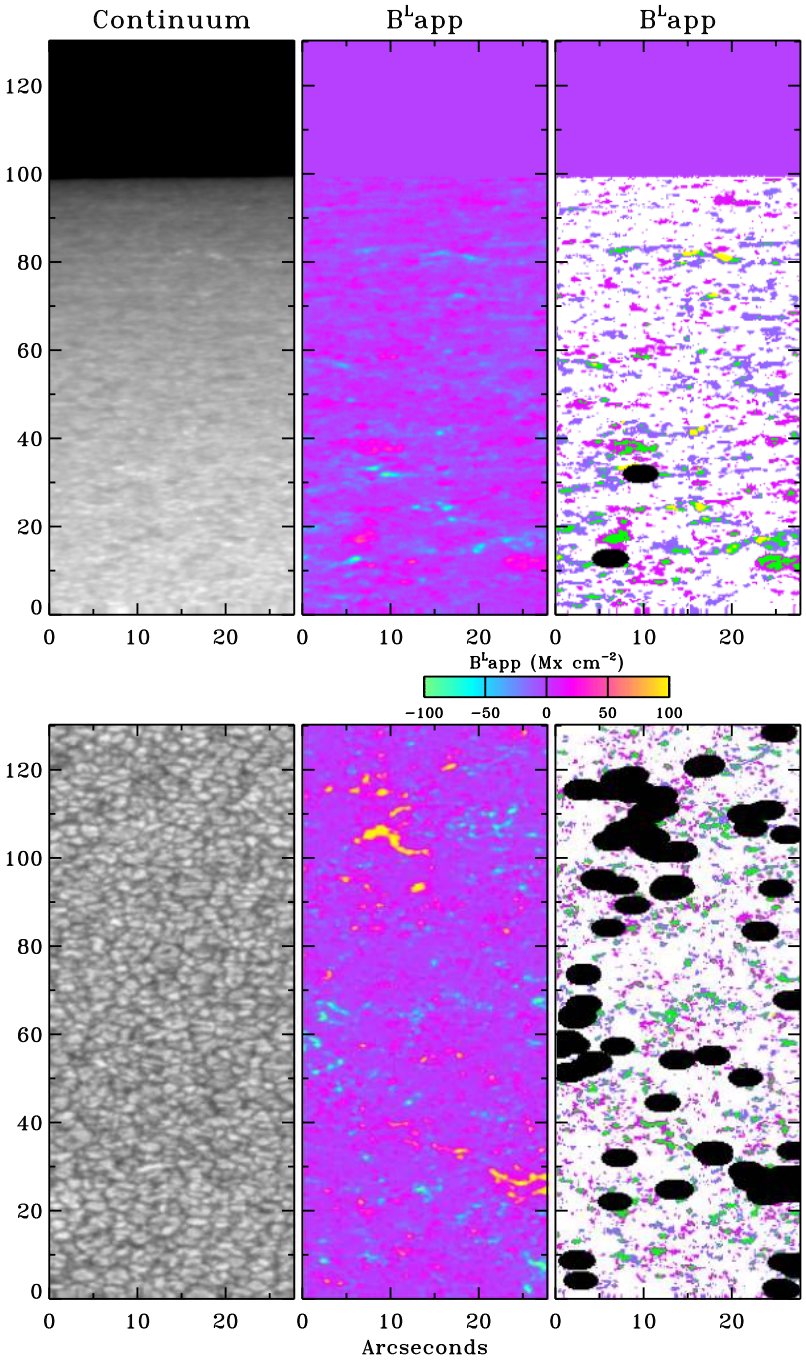

Fig. 3. The selection of quiet IN regions is illustrated for disk center (lower panels) and north limb (upper panels) HOP 79 SOT/SP data obtained on 2008 December 17 at 00:04 and 05:43 UT, respectively. Images are displayed with the as-observed unequal pixel sampling (see section 2). Panels display as follows: left: continuum intensity on gray scale; middle: longitudinal apparent flux density $B^L_{\rm app}$ with indicated color scale; right: $B^L_{\rm app}$ on the color scale with regions of $20 \le |B^L_{\rm app}| \le 100\,{\rm Mx\,cm^{-2}}$ flagged with green (Core IN), $B^T_{\rm app} > 170\,{\rm Mx\,cm^{-2}}$ flagged with yellow, Noise regions flagged with white, and Bloom regions flagged with black.

the displays of figure 4 excludes the pixels in the $3\,\sigma$ noise regime $|B^L_{\rm app}| < 7.2\,{\rm Mx\,cm^{-2}}$ (the white pixels in figure 3). The images in this figure are indexed in one-degree increments in latitude (or disk angle), and monthly in time. The disk angle is the angle between rays passing through the center of the Sun to the observer, and to the observed point on the solar disk, with the sign of the disk angle indicating the hemisphere of observation. The color scale presents the average $|B^L_{\rm app}|$ over all on-disk pixels falling within the specified latitude–time interval that have signal above the noise threshold, but subject to the constraints indicated for each image. For the few monthly periods having no sample,

a linear interpolation in time is performed between adjacent monthly intervals.

Panel (a) of figure 4 presents the average inferred $|B^L{}_{\rm app}|$ for all pixels above the 3σ noise threshold. The signature of the global solar cycle is clearly apparent in the activity belt between solar latitudes $\pm 40^\circ$. It should be remembered that observations are carried out on average only once per month for a very small window along the N–S meridian. Five of the 990 maps have sunspots, and another 11 of the maps have easily recognizable pores or plage as evidenced by the presence of disturbed granulation. Very weak pores or dark intergranular lanes are present in 11 more maps that have minimum continuum intensities less than 75% of the average for the map. As a consequence, very few of the observations actually intersect with active regions, so most of the high signals in the activity belt arise from remnants of active regions. For this reason the synoptic map in figure 4a does not show the butterfly diagram effect as distinctly as presented by figure 1, which is derived from daily full-disk measurements.

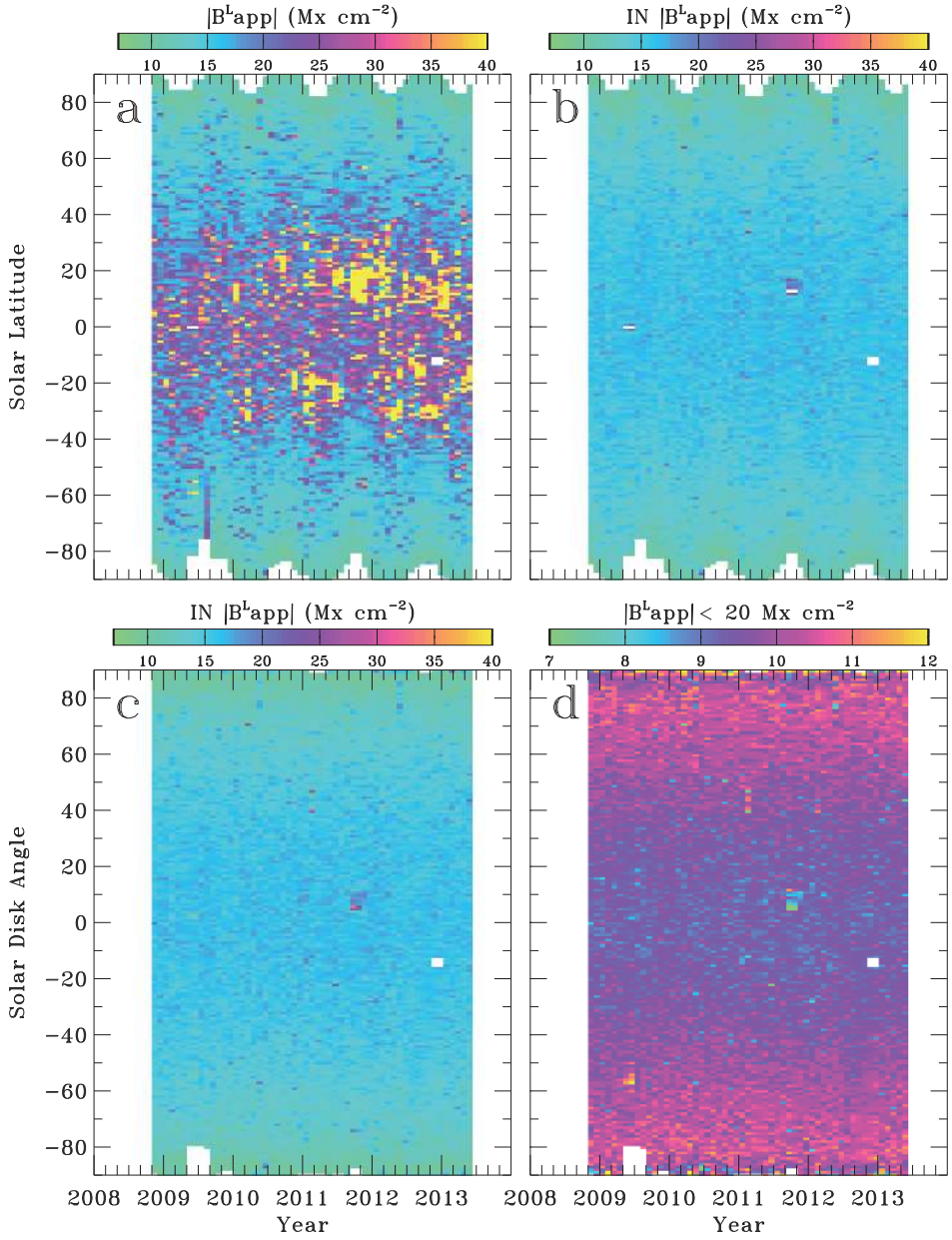

Fig. 4. Synoptic diagrams of the unsigned longitudinal apparent flux density $|B^L{}_{\rm app}|$ as a function of time and latitude (or disk angle) are presented for selected ranges of measured polarization. The color display represents the mean of $|B^L{}_{\rm app}|$ for pixels falling within each latitude/time bin having signals $> 3\sigma$ ($7.2\,{\rm Mx\,cm^{-2}}$) noise limit. (a) all longitudinal flux. (b) IN longitudinal flux (excluding areas flagged black or yellow in figure 3). (c) as (b), but displayed vs. disk angle (see text) rather than solar latitude. (d) as (c), but limited to flux elements with $|B^L{}_{\rm app}| < 20\,{\rm Mx\,cm^{-2}}$, Weak IN (note different color scale).

Figure 4b we display the unsigned IN longitudinal apparent flux density; that is, the average of all pixels above the noise threshold with $|B^L{}_{\rm app}| < 100\,{\rm Mx\,cm^{-2}}$ and excluding the bloom regions around stronger flux elements. Furthermore, the high-strength transverse fields, $B^T{}_{\rm app} > 170\,{\rm Mx\,cm^{-2}}$, as flagged in yellow in figure 3, are excluded. This latter criterion excludes some, but not all, strong vertical flux elements near the poles, but it has almost no effect for regions near disk center. For this measure of IN fields displayed in figure 4b, no trace of the global activity cycle remains. This result is consistent with the results of Buehler, Lagg, and Solanki (2013), who found little solar cycle dependence of the weak IN flux observed near disk center. The present work extends that result of their study to all solar latitudes. However, two effects are apparent in figure 4b: a marked increase in the average $|B^L{}_{\rm app}|$ toward the poles and an annual oscillation of the amplitude. The latter effect evidently results from display versus solar latitude, as verified by the equivalent display versus disk angle in figure 4c, where the annual variation, resulting from the variation of the B-angle, is absent. Thus we infer that this increase of IN $|B^L{}_{\rm app}|$ toward the poles is a center–limb effect, not a latitudinal effect.

Figure 4d displays our measure of the weakest component of IN longitudinal flux: the average $7.2 < |B^L{}_{\rm app}| < 20\,{\rm Mx\,cm^{-2}}$. This is the same measure for Weak IN adopted by Lites (2011). In that work it was also noticed that the Weak IN increased toward the limb, in contrast to the decrease toward the limb seen in figures 4b and 4c.

6 Synoptic maps for signed longitudinal apparent flux density

Figure 5 shows the measure of signed $B^L{}_{\rm app}$, corresponding to the white outline in the magnetic butterfly diagram of figure 1. The dynamic range of this display is smaller by a factor of two than that of figure 4 owing to the high degree of flux cancellation within each spatial-temporal bin. Figure 5a on the left shows the result for the average $B^L{}_{\rm app}$ for all pixels above the noise threshold. The sunspot activity belts at mid-latitudes are clearly visible. Also visible in figure 5a, and particularly in the IN and Weak IN flux averages shown in the rightmost two panels, is the progressive reversal of the negative polarity (blue) flux in the north polar region during 2011 and later. The south polar region appears to favor slightly positive flux (orange). This behavior also is consistent with the magnetic butterfly diagram of figure 1. We note preference for positive (negative) polarity at mid-north (mid-south) latitudes (20°–60°), especially for the Weak IN, figure 5c. This behavior corresponds to the "rush to the poles" of flux with polarity opposite to the dominant polar polarity at each pole, as is clearly visible in figure 1.

Figure 6 shows the dependence of the signed and unsigned apparent longitudinal flux density as a function of solar disk angle (not latitude), averaged over the entire time interval of these observations. The upper curves for $|B^L{}_{\rm app}|$ are indicated in blue for the selected IN flux, and in red for Weak IN, and the corresponding averages for signed $B^L{}_{\rm app}$ are presented in the lower curves, along with the rms fluctuation (in time among each of the monthly time bins of this display) for both IN and Weak IN. This display ratifies the visual impression from comparison of figures 4 and 5 that the average unsigned flux of the IN regions is considerably larger than that of the signed flux. In other words, the IN regions have nearly balanced positive and negative flux. This result agrees with the conclusions of Lites (2002, 2011) that most of the IN areas remain closely in balance even in enhanced network or weak plage regions where the stronger field components are significantly out of balance. However, figure 6 demonstrates that the IN, and even the Weak IN, regions near the poles harbor detectable polarity imbalance; a property well known when considering all flux elements (e.g., figure 1). Shiota et al. (2012) reported that the flux imbalance of the polar regions results primarily from the strong, vertically oriented, mainly unipolar flux elements, but that weaker elements tended toward flux balance. Examination of the flux density histograms of Shiota et al. (2012) for various epochs reveal what appear to be small but significant polarity imbalance for patches having flux $>10^{16}$ Mx, in agreement with the results in figure 5.

7 Synoptic maps for transverse apparent flux density

The synoptic diagrams for the measure of flux transverse to the line-of-sight, $B^T{}_{\rm app}$, are presented in figure 7. For this measure we exclude regions having linear polarization less than the $4\,\sigma$ continuum noise level in the vicinity of the limb; that is, we reject samples having $B^T{}_{\rm app} < 89\,{\rm Mx\,cm^{-2}}$. The measure of all transverse flux in panel (a) shows much less influence of the global solar cycle than do the corresponding longitudinal flux diagrams of figures 4 and 5. That the network elements appear unremarkable in images of quiet Sun linear polarization near disk center has been noted in several studies (Lites et al. 1996; Lites 2002; Lites et al. 2008; Ishikawa & Tsuneta 2009). Away from disk center the vertical network elements appear as fields transverse to the line-of-sight, hence the linear polarization signature increases. Because of this, the measure $B^T{}_{\rm app}$ in figure 7a "brightens" considerably toward the poles owing primarily to these network elements viewed transversely (Lites 2002). That behavior is less pronounced in the IN

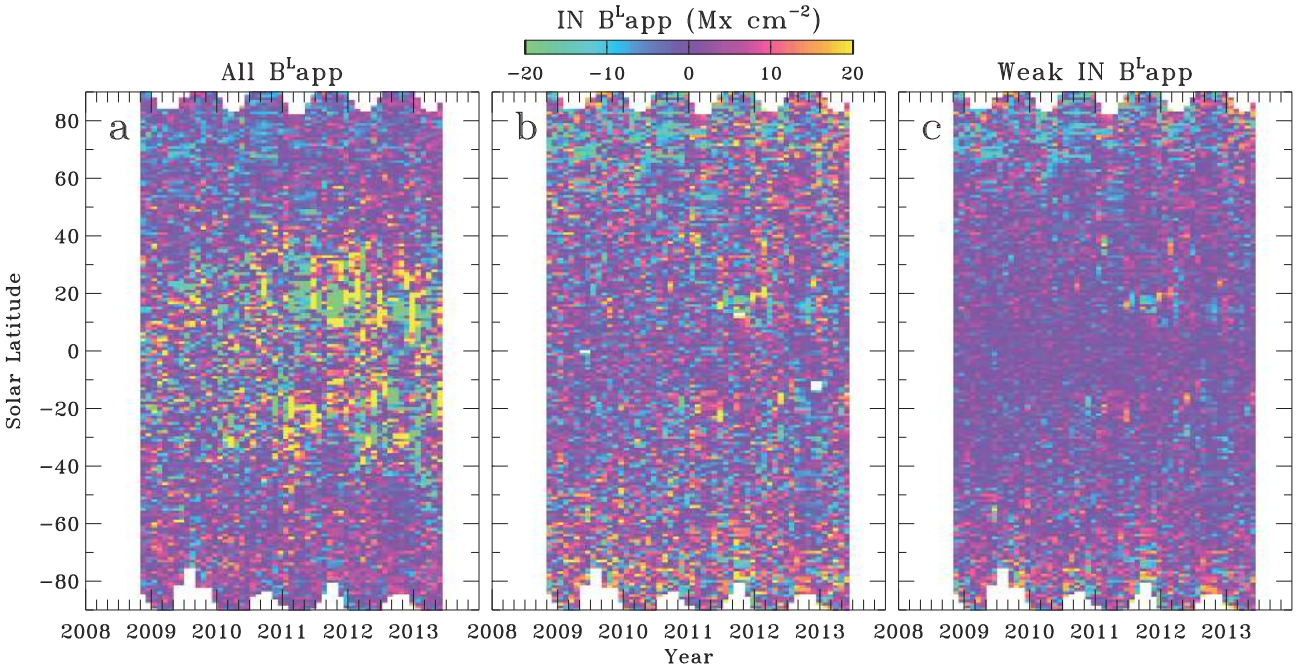

Fig. 5. Synoptic diagrams of the signed longitudinal apparent flux density B^L_{app} as a function of time and latitude are presented for selected ranges of measured polarization. Color display represents the mean of B^L_{app} for pixels falling within each latitude/time bin having signals $> 3\sigma$ (7.2 Mx cm^{-2}) noise limit. (a) all longitudinal flux. (b) IN longitudinal flux (excluding areas flagged yellow and black in figure 3). (c) as (b), but limited to flux elements with $|B^L_{app}| < 20$ Mx cm^{-2}.

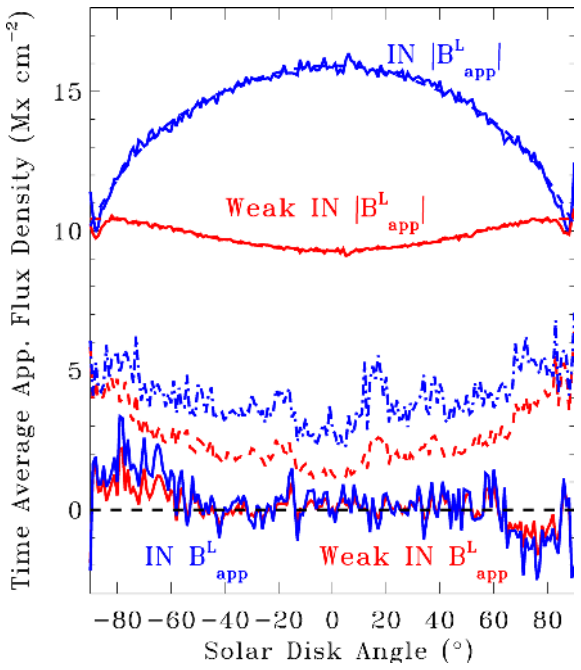

Fig. 6. Plotted in blue and red are measures of the time-averaged IN and Weak IN B^L_{app}, respectively. The upper two curves are unsigned flux density ($|B^L_{app}|$), with dashed lines showing smoothed fits to these "limb darkening" curves for measures of the field. The lower curves are for signed flux density B^L_{app} with dashed curves indicating the corresponding 1σ rms fluctuation in time at each disk angle. The black dashed line indicates the zero level.

B^T_{app} diagram of figure 7b because most of the network elements are avoided in the selection of IN. Near the poles we note some remaining enhancement of B^T_{app}. As noted in subsection 4.3, our network selection criterion $|B^L_{app}| < 100$ Mx cm^{-2} fails to isolate and avoid all strong-field patches near the limb. The remaining increase of B^T_{app} visible at the poles in figure 7b is attributable to the under-identification of these network patches there. The annual variation of this pattern reveals the effect to be a result of viewing angle, not solar latitude, as demonstrated by figure 7c where the IN B^T_{app} is displayed versus disk angle. In that figure the degree of enhancement of fields in the polar regions appears to diminish slightly with time, especially in the north polar region. That behavior is consistent with the reduction in north polar negative polarity flux in figure 5. We also note in figure 7c the slight decrease of IN B^T_{app} away from disk center to a disk angle of about 30°–40°, then an increase toward the poles. A possible scenario for this behavior is presented near the end of section 8.

8 Scenarios for the center–limb behavior

While the IN magnetic fields have very little variation with the solar cycle, the measures of IN flux presented herein show significant center–limb variations. These variations

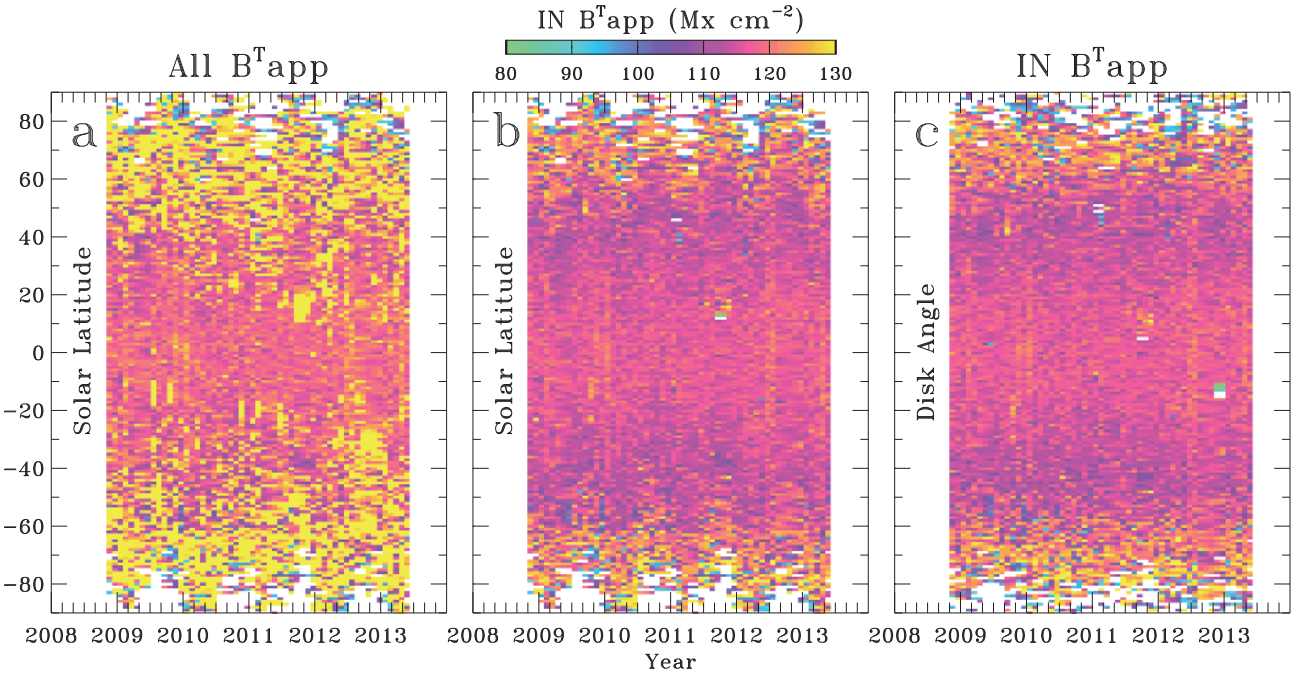

Fig. 7. The transverse apparent flux density B^T_{app} is presented in synoptic maps similar to those of the longitudinal fields shown in figures 4 and 5. Pixels below the noise threshold ($B^T_{app} < 89\,\mathrm{Mx\,cm^{-2}}$) are excluded from the averages in each latitude/time bin. Panels (a) and (b) display the distribution of all B^T_{app} and the IN B^T_{app}, respectively, versus solar latitude. The IN regions are isolated based on the longitudinal and transverse signals as described in subsection 4.3. Panel (c) displays IN B^T_{app} versus disk angle, not latitude.

with disk angle have been noted in prior studies. Lites et al. (2008) demonstrated that the IN$|B^L_{app}|$ decreases toward the limb. Lites (2011) noted a transition from "limb darkening" for the IN $|B^L_{app}|$ to "limb brightening" for Weak IN, as is evident from the top two curves in figure 6. Figure 4 demonstrates that this behavior does not depend on the phase of the solar cycle. It should be noted that our analysis yields averages over resolution elements along the central meridian per degree of either latitude or disk angle. As such, these presentations compensate for the effects of areal foreshortening, so that they represent averages over equal areas on the solar surface anywhere from the equator to the poles.

The sketch presented in figure 8 illustrates a possible explanation for the decrease of IN $|B^L_{app}|$ toward the limb. That diagram, adapted from Keller et al. (2004), illustrates the center–limb behavior of the visibility of a vertical, kilogauss flux tube having a significant Wilson depression of a few hundred kilometres. Note that Wilson depressions of the order of 200 km are associated with the simulated facular concentrations considered by Keller et al. (2004), and that these flux tube depressions have long been recognized as the source of facular brightness enhancement when viewed near the limb (the "bright wall" effect: Spruit 1976). When viewed close to the center of the disk, both the center of the flux tube (strong fields, green) and the fluted sides of the tube (magenta) are visible. When viewed close to the limb, the central, strong-field core is obscured by the optical depth of the disk-center side of the tube. The magnetic field signature will be smaller both because of the decrease of field strength in the fluted sides, and also because optical depth unity occurs higher in the atmosphere when viewed at an oblique angle. This scenario hinges on the presence of a significant Wilson depression in the IN flux elements, which in turn suggests that they harbor intrinsically strong magnetic fields.

Lites (2011) postulated that the increase away from disk center of $|B^L_{app}|$ for Weak IN may arise from the horizontal IN fields (Lites et al. 1996; Harvey et al. 2007; Lites et al. 2008) because of the dominance of horizontal fields in the upper photosphere (Lites et al. 2008; Schüssler & Vögler 2008; Steiner et al. 2009). A non-uniform angular distribution of magnetic fields was also inferred by Borrero and Kobel (2013) through study of the center–limb variation of observed distribution functions for circular and linear polarization. That the weak IN horizontal fields play a significant role is reinforced by the study of Ito et al. (2010), who compared properties of the magnetic fields observed at the poles and in the quiet Sun near the equator. They found the distributions of horizontal fields to be identical in the two regions. Evidently the imbalanced strong fields near the poles have little influence on the horizontal fields there, at least for the selection threshold for inversion adopted by Ito et al. (2010).

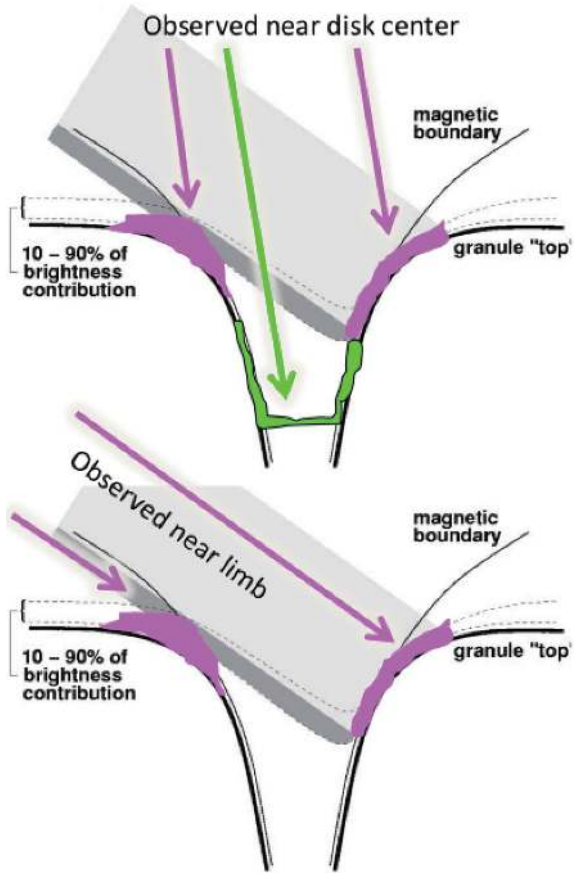

Fig. 8. Sketch of a possible explanation for the center–limb behavior of the weak IN magnetic fields. Top: network element viewed near the center of the disk. Bottom: polar facula viewed near the limb. Green and magenta areas represent Core IN and Weak IN contributors, respectively. This figure is adapted from figure 4 of Keller et al. (2004).

An alternate explanation might be afforded by noting in figure 3 that a significant fraction of the Weak IN signal at disk center arises from the regions surrounding the Core IN regions (displayed as green). Using figure 8 as an illustration, the magenta surroundings to the Core IN regions will have fields that are more horizontally oriented, so at the limb the line-of-sight component of these surroundings will be enhanced. The small density scale height in the photosphere causes very small, intense flux tubes to decrease rapidly in strength with height as the field lines spread in the horizontal direction forming a local magnetic canopy. Numerical modeling may be needed to determine if small-scale flux tubes can produce the observed center–limb behavior under this scenario. The near equality of Weak IN and IN $|B^{L}{}_{\rm app}|$ at the limb (see figure 6) arises naturally from this scenario because only the surroundings of the flux tubes are visible there.

With these data, and our present knowledge of the IN magnetism, we do not see a way to determine which, if either, of the horizontal fields or the perspective effect scenarios is more likely.

A decrease of $B^{T}{}_{\rm app}$ away from disk center, but outside of the polar regions, is visible in figures 7b and 7c. From a small sample of Hinode SOT/SP observations with very high sensitivity during 2007, Lites et al. (2008) also reported a slight decrease of $B^{T}{}_{\rm app}$ not only away from disk center, but continuing to the limb as well. Those results comprised all linear polarization signals observed above a 2 σ noise level, not just those we identify here as IN. The areal coverage included in the analysis of an individual map of that work is much greater than that of the present work owing to the much deeper exposures, as witnessed by comparison of figure 3 with figure 11 of Lites et al. (2008). We speculate that their much deeper exposures reveal many more weak transverse elements than are selected as IN as presented in figure 7, thereby skewing the distribution toward lower average $B^{T}{}_{\rm app}$.

Away from the polar regions, the measures of $B^{T}{}_{\rm app}$ in figures 7b and 7c should have only a small influence from the projection of vertically oriented strong-field patches onto the plane transverse to the line-of-sight because regions of both strong linear and circular polarization are avoided in our IN selection (see subsection 4.3). The small-scale horizontal fields in the solar photosphere that appear prominently in images of the quiet Sun linear polarization (figure 2 of Lites et al. 2008, for example) must dominate the signals of figures 7b and 7c outside of the polar regions. The decrease of the signal away from the center of the disk suggests that the magnetic fields of the IN are not isotropically distributed, but are in fact dominated by horizontal fields.

9 Conclusions and discussion

The primary observational results from this study are as follows:

(i) The *unsigned* longitudinal apparent flux density $|B^{L}{}_{\rm app}|$ in internetwork regions does not reveal signatures of the global solar cycle. This result holds for IN and Weak IN selections alike—see figures 4b–4d.

(ii) In IN and Weak IN regions the *signed* $B^{L}{}_{\rm app}$ contains signatures of the large-scale solar cycle patterns apparent in figure 1: the polarity imbalance and its time variation near the poles, and possibly signatures of unipolar flux at latitudes between the sunspot emergence zones and the poles. However, these signatures are significantly smaller than the unsigned IN and unsigned Weak IN $|B^{L}{}_{\rm app}|$.

(iii) The transverse apparent flux density $B^{T}{}_{\rm app}$ also reveals no large-scale solar cycle dependence for the selected IN regions.

(iv) Distinct signatures exist for the center–limb variation of $|B^L{}_{\rm app}|$ in both IN and Weak IN selected regions, and for $B^T{}_{\rm app}$ in IN.

From these observational results, we draw the following conclusions:

(i) For our selection of internetwork regions, the general absence in $|B^L{}_{\rm app}|$ of the large-scale patterns seen in figure 1 is consistent with the continual operation of a small-scale dynamo process in those regions.
(ii) The weak signature of the solar cycle that persists in the *signed* $B^L{}_{\rm app}$ still needs to be understood. We offer some possible explanations in the following discussion.
(iii) The center–limb variation of $|B^L{}_{\rm app}|$ in the IN and Weak IN may both be understood in terms of compact flux tubes viewed obliquely. For the Weak IN, alternatively (or additionally) the known dominance of horizontal fields over vertical ones in the internetwork might produce the same behavior.
(iv) The initial decrease away from disk center of $B^T{}_{\rm app}$ in the IN at low to mid-latitudes might also be understood in terms of the dominance of horizontal fields in the upper photosphere.

That the results of this study are consistent with the operation of a small-scale dynamo in all quiet Sun regions agrees with the several other studies to date of IN magnetism (Ishikawa & Tsuneta 2009; Lites 2011; Buehler et al. 2013). Taken as a group these results are strong circumstantial evidence for the the operation of a small-scale dynamo, but of course they do not prove its presence conclusively.

The clear signature of the large-scale polar magnetic cycle in figures 5b, 5c, and the hint of the large-scale patterns at mid-latitudes in those diagrams, might be an artifact of the selection process for IN and Weak IN. We noted in subsection 4.3 that our criterion for isolation of the network patches, $|B^L{}_{\rm app}| > 100\,{\rm Mx\,cm^{-2}}$ and their surroundings, does not isolate some of the stronger polar network patches (note the green and yellow regions in the upper-right panel of figure 3). Even considering only the Weak IN selection, it is possible that some of the instrumental polarization bloom around those unipolar strong fields near the poles that have not been de-selected (i.e., not obscured by black) may be retained, thus retaining some fraction of the net polarity imbalance seen in figure 5c. Alternatively, there may be an explanation of this behavior that is solar in origin. Lateral diffusion of flux away from stronger-field concentrations may spread the imbalance of polarities to the surrounding internetwork regions. From an observational standpoint, however, this effect cannot be very strong as Lites (2011) noted that the overall polarity imbalance of internetwork regions is only weakly correlated with the net local imbalance of all magnetic flux.

We have offered a scenario for the observed center–limb behavior of IN$|B^L{}_{\rm app}|$ that relies upon the presence of small-scale flux concentrations. Close examination of the lower-right panel of figure 3 shows that very many of the IN flux elements are small, stronger-field Core IN elements (green) surrounded by the Weak IN regions (magenta). This observed behavior renders the scenario of figure 8 more plausible, but the question remains as to the presence of a significant Wilson depression for these small IN flux elements. It is nearly certain that many of these small features remain unresolved, perhaps by large factors, in this Hinode SOT/SP data. The debate continues regarding the distribution of intrinsic strengths of unresolved magnetic fields in the photosphere. Recently, Stenflo (2011; see also Stenflo 2013) argued the case for a distribution containing a significant proportion of intense-field flux tubes at very small scales. These results were based on the ratio of Stokes V amplitudes in the Fe I line pair at 630 nm as observed by Hinode SOT/SP, whereby in the strong-field limit the ratio approaches a fixed value. However, from Stokes spectra from MHD simulations, Steiner and Rezaei (2012) demonstrated that such large Stokes V ratios arise naturally from a magnetic canopy surrounding field concentrations of a few hundred gauss, not from tiny kilogauss flux tubes. Considering other diagnostics of the IN magnetic fields, Orozco Suárez and Katsukawa (2012) also concluded that the intrinsic field strengths in these concentrations are indeed of the order of a few hundred gauss. So how do we reconcile the scenario of figure 8 in the absence of strong, very small-scale kilogauss flux tubes? Perhaps the answer will come from simulations such as those analyzed by Steiner and Rezaei (2012). If the dominant flux concentrations having field strengths of a few hundred gauss produce surrounding canopy fields, then it is possible that these canopies dominate the visibility of our selected Weak IN regions when viewed near the limb. Indeed, the dominance of horizontal fields in the quiet IN may also be thought of as a canopy. At this time we believe that guidance from numerical MHD simulations of magneto-convection in the solar photosphere is necessary to understand the observed center–limb variations outlined in this work. The first step would be to verify that synthetic observations derived from recent generations of realistic MHD simulations reproduce the center–limb behavior of the weakest observable components of IN flux. If similar trends are noted in the synthetic data one could then examine the simulations in detail to verify or refute the scenarios presented herein.

From a small sample of Hinode SOT/SP observations with very high sensitivity during 2007, Lites et al. (2008) reported a slight decrease of $B^T{}_{\rm app}$ away from disk center,

and even near the limb. Those results comprised all linear polarization signals observed above a 2 σ noise level, not just those we identify here as IN. The fractional areal coverage selected from those long exposures is much greater than that of the present work, as witnessed by comparison of figure 3 with figure 11 of Lites et al. (2008). We speculate that the much deeper exposures of that work would reveal many more weak transverse elements than are selected as IN as presented in figure 7, thereby skewing the distribution toward lower average $B^T{}_{\rm app}$.

Acknowledgments

We thank the many other individuals in the USA and Japan for their dedicated work throughout development of the Hinode mission, and also those involved with the mission after launch. We also thank R. Casini for reviewing the manuscript and providing many helpful comments and suggestions, and an anonymous referee whose comments helped improve the manuscript. Hinode is a Japanese mission developed and launched by ISAS/JAXA, collaborating with NAOJ as a domestic partner, NASA and STFC (UK) as international partners. Scientific operation of the Hinode mission is conducted by the Hinode science team organized at ISAS/JAXA. This team mainly consists of scientists from institutes in the partner countries. Support for the post-launch operation is provided by JAXA and NAOJ (Japan), STFC (UK), NASA, ESA, and NSC (Norway). The FPP project at LMSAL and HAO is supported by NASA contract NNM07AA01C. The National Center for Atmospheric Research is sponsored by the National Science Foundation.

References

Babcock, H. W. 1961, ApJ, 133, 572
Borrero, J. M., & Kobel, P. 2013, A&A, 550, A98
Buehler, D., Lagg, A., & Solanki, S. K. 2013, A&A, 555, A33
Harvey, J. W., Branston, D., Henney, C. J., & Keller, C. U. 2007, ApJ, 659, L177
Hathaway, D. H. 2010, Living Rev. Sol. Phys., 7, 1
Howard, R., & Labonte, B. J. 1981, Sol. Phys., 74, 131
Hyder, C. L. 1965, ApJ, 141, 272
Ishikawa, R., & Tsuneta, S. 2009, A&A, 495, 607
Ito, H., Tsuneta, S., Shiota, D., Tokumaru, M., & Fujiki, K. 2010, ApJ, 719, 131
Judge, P. G., Elmore, D. F., Lites, B. W., Keller, C. U., & Rimmele, T. 2004, Appl. Opt., 43, 3817
Keller, C. U., Schüssler, M., Vögler, A., & Zakharov, V. 2004, ApJ, 607, L59
Kleint, L., Berdyugina, S. V., Shapiro, A. I., & Bianda, M. 2010, A&A, 524, A37
Kosugi, T., et al. 2007, Sol. Phys., 243, 3
Leighton, R. B. 1964, ApJ, 140, 1547
Lites, B. W. 1987, Appl. Opt., 26, 3838
Lites, B. W. 2002, ApJ, 573, 431
Lites, B. W. 2011, ApJ, 737, 52
Lites, B. W., et al. 2008, ApJ, 672, 1237
Lites, B. W., et al. 2013, Sol. Phys., 283, 579
Lites, B. W., & Ichimoto, K. 2013, Sol. Phys., 283, 601
Lites, B. W., Leka, K. D., Skumanich, A., Martinez Pillet, V., & Shimizu, T. 1996, ApJ, 460, 1019
Orozco Suárez, D., & Katsukawa, Y. 2012, ApJ, 746, 182
Sánchez Almeida, J. 2003, A&A, 411, 615
Schüssler, M., & Vögler, A. 2008, A&A, 481, L5
Shchukina, N., & Trujillo Bueno, J. 2003, in ASP Conf. Ser., 307, Solar Polarization, ed. J. Trujillo-Bueno & J. Sanchez Almeida (San Francisco: ASP), 336
Shimizu, T., et al. 2008, Sol. Phys., 249, 221
Shiota, D., Tsuneta, S., Shimojo, M., Sako, N., Orozco Suárez, D., & Ishikawa, R. 2012, ApJ, 753, 157
Spruit, H. C. 1976, Sol. Phys., 50, 269
Steiner, O., & Rezaei, R. 2012, in ASP Conf. Ser., 456, Fifth Hinode Science Meeting, ed. L. Golub et al. (San Francisco: ASP), 3
Steiner, O., Rezaei, R., Schlichenmaier, R., Schaffenberger, W., & Wedemeyer-Böhm, S. 2009, in ASP Conf. Ser., 415, The Second Hinode Science Meeting: Beyond Discovery – Toward Understanding, ed. B. Lites et al. (San Francisco: ASP), 67
Stenflo, J. O. 2011, A&A, 529, A42
Stenflo, J. O. 2013, A&AR, 21, 66
Tsuneta, S., et al. 2008, Sol. Phys., 249, 167
Ulrich, R. K., & Tran, T. 2013, ApJ, 768, 189
Waldmeier, M. 1960, Z. Astrophy., 49, 176
Wang, Y.-M., Nash, A. G., & Sheeley, N. R., Jr. 1989, ApJ, 347, 529